

Received November 12, 2020, accepted November 28, 2020, date of publication December 3, 2020, date of current version December 28, 2020.

Digital Object Identifier 10.1109/ACCESS.2020.3042207

Image-Based Visual Servoing Control of Robot Manipulators Using Hybrid Algorithm With Feature Constraints

XIAOLIN REN^{1,2,3}, HONGWEN LI^{1,2}, AND YUANCHUN LI³

¹Changchun Institute of Optics, Fine Mechanics and Physics, Chinese Academy of Science, Changchun 130033, China

²University of Chinese Academy of Science, Beijing 100049, China

³Department of Control Science and Engineering, Changchun University of Technology, Changchun 130012, China

Corresponding author: Xiaolin Ren (xlren1985@ccut.edu.cn)

This work was supported in part by the National Natural Science Foundation of China under Grant 61773075 and Grant 61703055, in part by the Scientific Technological Development Plan Project in Jilin Province of China under Grant 20200801056GH and Grant 20190103004JH, and in part by the Science and Technology Project of the Jilin Provincial Education Department of China during the 13th Five-Year Plan Period under Grant JJKH20200672KJ, Grant JJKH20200673KJ, and Grant JJKH20200674KJ.

ABSTRACT The challenge in addressing uncalibrated visual servoing (VS) control of robot manipulators with unstructured environments is to obtain appropriate interaction matrix and keep the image features in the field of view (FOV), especially when the non-Gaussian noise disturbance exists in the VS process. In this article, a hybrid control algorithm which combines bidirectional extreme learning machine (B-ELM) with smooth variable structure filter (SVSF) is proposed to estimate interaction matrix and tackle visibility constraints. For VS, the nonlinear mapping between image features and interaction matrix is approximated using the B-ELM learning. To increase the capability of anti-interference, the SVSF is employed to re-estimate interaction matrix. A constraint function presenting feature coordinates and region boundaries is given and added to the velocity controller, which drags image features away from the restricted region and ensures the smoothness of the velocities. Since the camera and robot model parameters are not required in developing the control strategy, the servoing task can be fulfilled flexibly and simply. Simulation and experimental results on a conventional 6-degree-of-freedom manipulator verify the effectiveness of the proposed method.

INDEX TERMS Bidirectional extreme learning machine, smooth variable structure filter, constraint function, restricted region, visual servoing.

I. INTRODUCTION

Visual feedback signals have been used as significant information in robots to tackle the positioning or motion control in unstructured environments. Different from the traditional visual servoing (VS) system requiring professional calibration, a challengeable task with higher flexibility and adaptability is to face uncertain disturbances and features escaping from the image plane for uncalibrated systems, especially in robot positioning and trajectory tracking control. To pursue high control efficiency, convenient application and good performance become important developing direction in the field of visual servoing.

The associate editor coordinating the review of this manuscript and approving it for publication was Thomas Canhao Xu.

VS employs visual features of the target object to generate the robot control policy so as to guarantee the error within an allowable domain. According to the visual feedback signal returned by 3D Cartesian space coordinate or image plane coordinate, it can be divided into position-based visual servoing (PBVS), image-based visual servoing (IBVS) and hybrid visual servoing control systems [1]–[3]. Generally speaking, the PBVS is highly dependent on the calibrated camera and the accurate geometric model for reconstructing the relative pose of the object. However, accurate calibration is difficult. Meanwhile, since the signal of image features lies outside the control loop, the target might also lie out of the view field. IBVS refers to the feedback control strategy is designed directly according to the error signals defined by the image features. It needs to calculate the image Jacobian matrix and its inverse matrix, i.e., to determine the

relationship between the change of image feature parameters and robot pose. In IBVS, the analytical form of the image Jacobian matrix is obtained in the control loop which requires accurate calibration of camera model parameters. However, the 3D parameter information cannot be measured directly, and the external camera calibration with respect to the end-effector is required. It makes the calibration of VS system subject to many limitations in practical applications, such as the degradation of camera parameters, and the large calibration error caused by small changes in the unstructured environment. An uncalibrated IBVS, which does not require scene model or camera/robot calibration, applies image feature information (e.g., point feature, line feature and image moment) to estimate the unknown system dynamics, and then the controller is designed based on the identified Jacobian matrix [4], [5]. Therefore, the uncalibrated-based methods have stronger robustness to calibration errors, and become potential and active research areas [6]–[8].

For kinematic uncalibrated VS systems, the control performance mainly depends on the speed and precision of on-line estimation of Jacobian matrix. The operation accuracy is not only affected by model and parameter uncertainties, but also by noise and external disturbance. Some existing works based on Jacobian matrix have been reported for nonlinear optimization and state estimation, such as Broyden and its improved method [9]–[12], recursive least squares [13]–[15], Levenberg-Marquadt [16], [17], support vector regression (SVR) [18], Kalman filter (KF) [19], and particle filtering (PF) [20]. Music *et al.* [10] systematically compared the performance of dynamic Broyden-Gauss-Newton method, group-based Broyden method, KF method and PF method, and summarized that these algorithms have their own shortcomings in calculating speed or dealing with environmental noise. In [21], the Geman-McClure estimator was selected to adjust the objective function to allocate weights and improve the estimation accuracy of the Jacobian matrix. In [22], Sagu-Husa adaptive KF was applied to the online state estimation of image Jacobian, and the filter parameter was adjusted to improve the adaptive ability of Jacobian identification model under partial known noises. Zhong *et al.* used Kalman-neural-network filter to minimize the estimation error of the interaction matrix, and discussed the influence of stochastic noise [23], [24]. Some other Jacobian matrix estimation approaches were proposed with neural networks. In [25], a hybrid genetic optimization BP neural network algorithm was presented to model the compound Jacobian matrix. Zhong *et al.* proposed an algorithm combining robust KF with Elman neural network to identify the interaction matrix online with considering the compound noise [26]. Both [27] and [28] employed extreme learning machine (ELM) to estimate the pseudoinverse of the interaction matrix to avoid matrix singularity and the noise. [29] established the interaction matrix between the time-variation of the wavelet coefficients and the spatial robot velocity and used the wavelet coefficients to obtain the control law.

In addition, to keep the image features in the field of view (FOV) is one of key points for the success of VS control. In order to avoid the failures of VS task caused by image disappearance, researchers presented different approaches. Mezouar and Chaumette [30] introduced a robust image-based potential field method for trajectory planning. In the proposed approach, camera FOV and robot joint limitations were considered. In [31], potential field-based strategies were applied to a global framework which took into account the field constraints and joint constraints. Ding *et al.* [32] proposed a path planning method based on hybrid artificial potential field to solve the field of vision constraint problem during operation. Chesi *et al.* [33] proposed to a FOV keeping system based on the switch control strategy and backward motion. [34] presented an online IBVS controller for a 6-degree-of-freedom (DOF) robot system based on the robust model predictive control method by taking into account the input and output constraints of robotic VS system, such as robot physical limitations and visibility constraints. The visibility constraints, parametric uncertainties and physical limitations can be easily transformed into nonequivalent constraints associated with the output and input of VS systems. Perez-Cisneros [35] presented an evolutionary optimization based predictive control strategy for VS systems. The visual control task was regarded as a nonlinear optimization problem with workspace and visual constraints. [36] proposed a visual servoing scheme that imposed predefined performance specifications on the image feature coordinate errors. It can guarantee the transient and steady performance, satisfy the FOV constraints and reduce the design complexity. [27] utilized a negative motion based on fuzzy logic to keeping FOV. Zhong *et al.* [23] proposed a Kalman neural network filter which compensated the nonlinear modeling error and the statistical noise, however, the FOV constraint was not adequately explained.

Although the uncalibrated VS does not need to calibrate the camera parameters in theory, the system performance will deteriorate during the servo process, such as complicated noisy environments and features escaped from the camera vision field can affect the convergence of the servo system or even lead to task failure. In this article, a method combined bidirectional extreme learning machine (B-ELM) algorithm with smooth variable structure filter (SVSF) algorithm was proposed to map the nonlinearity between the visual space of the robot manipulator and the motion space of the end-effector, and the FOV constraint was adopted to ensure that no feature points will be lost during the whole motion.

The main contributions of this article can be summarized as follows:

- 1) The B-ELM cooperated with SVSF is presented to estimate Jacobian matrix in uncalibrated VS. The SVSF is endowed to re-estimate output matrix of B-ELM which improves the robustness of the system in the presence of the non-Gaussian noisy environment.

2) Hyperelliptic boundary is adopted to smooth the boundary of the field of visual constraint in VS control. A novel constraint function is developed to dynamically adjust the servo controller via dividing the regions by different boundaries. It ensures that the image feature points are always visible during the movement.

The remainder of this article is organized as follows: Section 2 describes the hybrid Jacobian matrix estimation method in detail. In Section 3, the visual constraint strategy is developed. In Section 4, a novel framework of VS controller with constraints is proposed. In Section 5, experiments are provided to demonstrate the effectiveness of the developed method with respect to different noise conditions. Finally, a brief conclusion is provided in Section 6.

II. VISUAL SERVOING OF ROBOT MANIPULATORS

A. BACKGROUND

In this article, a camera which is mounted on the robot end-effector moves with robot manipulator. The main objective of VS control is to drive the robot end-effector with camera toward desired image features through robot joint movement. The image feature is directly used for controller design, and the image space error $e(k)$ at epoch k is defined as

$$e(k) = S(k) - S^*, \quad (1)$$

where $S(k) = [S_1(k), \dots, S_{m_s}(k)]^T \in \mathbb{R}^{m_s}$ is the vector of image features at time k , m_s is the number of image features, $S^* \in \mathbb{R}^{m_s}$ is the desired vector of features.

Let $r(k) = [r_1(k), \dots, r_{n_r}(k)]^T \in \mathbb{R}^{n_r}$ be the position and orientation of robot end-effector in Cartesian space and $n_r = 6$, $\dot{r}(k) = [v_x(k), v_y(k), v_z(k), \omega_x(k), \omega_y(k), \omega_z(k)]^T \in \mathbb{R}^6$ describes the corresponding velocity screw vector. The camera velocity is mapped to image feature by the feature Jacobian matrix (or interaction matrix), which can be expressed

$$\dot{S}(k) = J_I(k) \cdot \dot{r}(k), \quad (2)$$

where $J_I(k)$ is feature Jacobian matrix which can be computed by

$$\begin{aligned} J_I(k) &= \frac{\partial S(k)}{\partial r(k)} \\ &= \begin{bmatrix} \frac{\partial S_1(k)}{\partial r_1(k)} & \cdots & \frac{\partial S_1(k)}{\partial r_{n_r}(k)} \\ \vdots & \ddots & \vdots \\ \frac{\partial S_{m_s}(k)}{\partial r_1(k)} & \cdots & \frac{\partial S_{m_s}(k)}{\partial r_{n_r}(k)} \end{bmatrix}_{m_s \times n_r} \\ &= \begin{bmatrix} j_{11} & \cdots & j_{1n_r} \\ \vdots & \ddots & \vdots \\ j_{m_s 1} & \cdots & j_{m_s n_r} \end{bmatrix}_{m_s \times n_r}. \end{aligned} \quad (3)$$

In order to drive a robot from the current feature point to the desired feature point, the relationship between the time variable of the error and the camera velocity can be given by

$$\dot{r}(k) = -\lambda J_I^+(k) \cdot e(k), \quad (4)$$

where $J_I^+(k)$ is the pseudo-inverse of feature Jacobian matrix, and $\lambda > 0$ is a fixed control gain.

Before designing the VS controller, the system is supposed to satisfy the following assumptions.

Assumption 1: There is no transformation between the camera coordinate and end-effector coordinate with eye-in-hand configuration.

Assumption 2: Image feature points observed by camera are coplanar.

B. B-ELM FUNCTION APPROXIMATION METHOD

Unlike conventional ELM, B-ELM which refers to a variable of incremental extreme learning machine (I-ELM) was proposed by Yang *et al.* [37]. When the number of hidden nodes is odd, the hidden node parameters are generated randomly in accordance with I-ELM. However, when the number of hidden nodes is even, the hidden node parameters are determined by proper error functions. In this way, the hidden node can be added automatically until the model satisfies the given precision or the number of hidden nodes beyonds the given maximum. It was proved that B-ELM can greatly improve the learning efficiency, further reduce the number of hidden nodes and computational cost. The algorithm of B-ELM is provided in details as follows.

For M arbitrary distinct samples (x_j, y_j) , where $x_j \in \mathbb{R}^d$, $y_j \in \mathbb{R}^m$, the output function of ELM is

$$o_j(x) = \sum_{i=1}^L \beta_i g(a_i x_j + b_i), \quad a_i \in \mathbb{R}^n, b_i \in \mathbb{R}, \quad j = 1, \dots, M, \quad (5)$$

where β_i is the output weight vector between hidden and output layers, $g(\bullet)$ is activation function, o_j is the network output, a_i is the weight vector connecting the i th hidden node and the input nodes, b_i is the bias of the i th hidden node, L is the number of hidden nodes. If the network output is equivalent to the target, i.e., $\sum_{j=1}^M \|o_j - y_j\| = 0$, (5) can be rewritten as

$$y_j(x) = \sum_{i=1}^L \beta_i g(a_i x_j + b_i), \quad a_i \in \mathbb{R}^n, b_i \in \mathbb{R}, \quad j = 1, \dots, M. \quad (6)$$

And (6) can be written as

$$G\beta = Y, \quad (7)$$

where $Y = [y_1, \dots, y_M] \in \mathbb{R}^{M \times m}$ is target matrix, $\beta = [\beta_1^T, \dots, \beta_L^T] \in \mathbb{R}^{L \times m}$ is weight of output matrix and $G \in \mathbb{R}^{M \times L}$ is the hidden layer matrix as

$$G = \begin{bmatrix} g(a_1 \cdot x_1 + b_1) & \cdots & g(a_L \cdot x_1 + b_L) \\ \vdots & \ddots & \vdots \\ g(a_1 \cdot x_M + b_1) & \cdots & g(a_L \cdot x_M + b_L) \end{bmatrix}. \quad (8)$$

It is clear that the solution of the network can be obtained by the least-squares method. However, in most cases $M \neq L$,

the solution of (7) can be written as

$$\hat{\beta} = G^+ Y, \quad (9)$$

where G^+ denotes the pseudo-inverse matrix of G .

Based on the B-ELM algorithm, Yang *et al.* [37] provided a single hidden layer feedforward neural network (SLFN) with a bounded nonconstant piecewise continuous function $\mathbf{H} : \mathbf{R} \rightarrow \mathbf{R}$ for additive nodes or sine nodes. For any continuous target function f , randomly generates function sequence G_{2n+1}^r , and obtains error feedback function sequence G_{2n}^e , $n \in \mathbb{Z}$. $e_n = f - f_n$ is the residual error function for the current network f_n with n hidden nodes. Then, the number of hidden nodes $L \in \{2n+1, n \in \mathbb{Z}\}$, the hidden node parameter a_{2n+1} and b_{2n+1} are determined randomly by the I-ELM as

$$G_{2n+1}^r = G(a_{2n+1}, b_{2n+1}, x), \quad (10)$$

$$\beta_{2n+1} = \frac{\langle e_{2n}, G_{2n+1}^r \rangle}{\|G_{2n+1}^r\|^2}. \quad (11)$$

Along with the number of hidden nodes $L \in \{2n, n \in \mathbb{Z}\}$, the parameter a_{2n} and b_{2n} are obtained according to the formulas as

$$G_{2n}^e = e_{2n-1}(\beta_{2n-1})^{-1}, \quad (12)$$

$$a_{2n} = g^{-1}(U(G_{2n}^e)) \cdot x^{-1}, \quad (13)$$

$$b_{2n} = \sqrt{\text{mse}(g^{-1}(U(G_{2n}^e)) - a_{2n} \cdot x)}, \quad (14)$$

$$\hat{G}_{2n}^e = U^{-1}(g(a_{2n} \cdot x + b_{2n})), \quad (15)$$

$$\beta_{2n} = \frac{\langle e_{2n-1}, \hat{G}_{2n}^e \rangle}{\|\hat{G}_{2n}^e\|^2}, \quad (16)$$

where $U : \mathbf{R} \rightarrow [0, 1]$ is a normalized function, g^{-1} and U^{-1} represent the inverse functions of g and U , respectively. The algorithm of B-ELM is represented in Table 1.

The calculation of Jacobian matrix (or its pseudo-inverse) is very important in visual servoing control, which changes when the manipulator moves. It makes sense to approximate the Jacobian matrix effectively so as to reduce the computational cost of offline training and online application. In this article, B-ELM is employed to estimate $J_I(k)$. We set each element of $S(k)$ as the input, and each element of $J_I(k)$ as the target output. In order to use activation function more effectively, all input and output sample data should be normalized.

C. SMOOTH VARIABLE STRUCTURE FILTER STATE ESTIMATION

For kinematic uncalibrated visual servoing systems, explicit expression of image Jacobian matrix or interaction matrix cannot be provided without explicitly computing camera's internal and external parameters. The Jacobian matrix is regarded as the system state, and can be accurately estimated by the state estimation scheme. The standard KF method is highly dependent on the known statistical characteristics of noise, which is difficult to determine in the actual robot vision task. It may lead to the decrease or even divergence of filtering

TABLE 1. The algorithm of B-ELM.

Input: Given a training set $\{x_j, y_j\}_{j=1}^M$, the hidden layer mapping function $g(x)$, the hidden layer maximum junction number L_{max} and the training error ε .
Output: A trained B-ELM model.
Recursively growing phase:
-Let the initial hidden layer node be $L=0$, the network residual error matrix be $E = Y$.
-When $L < L_{max}$ and $\ E\ > \varepsilon$ do
-Set hidden nodes $L : L = L + 1$;
-if $L \in \{2n + 1, n \in \mathbb{Z}\}$, then
(i) assign random input weight a_{2n+1} and bias b_{2n+1} ;
(ii) calculate randomly generated function sequence G_{2n+1}^1 according to (10);
(iii) calculate the output weight β_{2n+1} according to (11);
else
(i) calculate error feedback function sequence G_{2n}^e according to (12);
(ii) calculate the input weight a_{2n} , bias b_{2n} according to (13) and (14);
(iii) calculate \hat{G}_{2n}^e according to (15);
(iv) calculate the output weight β_{2n} according to (16);
end
-calculate the residual error after adding the new hidden node $E = E - H_L \beta_L$.
end

accuracy. SVSF [40] is a predictor-corrector method based on sliding mode. As a new state estimation strategy, the effective improvement of SVSF is obtained in the presence of modeling uncertainties and noise. The basic estimation scheme of the SVSF is shown in Fig.1.

The discrete-time linear dynamical system can be expressed as:

$$X(k) = X(k - 1) + w(k), \quad (17)$$

$$Z(k) = H(k)X(k) + v(k), \quad (18)$$

where $X(k) = [j_{11}, \dots, j_{m_s n_r}]^T \in \mathbb{R}^{(m_s \times n_r) \times 1}$ is the state vector, $w(k) \in \mathbb{R}^{(m_s \times n_r) \times 1}$ and $v(k) \in \mathbb{R}^{m_s}$ are process noise and measurement noise, respectively, $Q(k)$ and $R(k)$ are the state model and measurement noise covariance matrix, $Z(k) \in \mathbb{R}^{m_s}$ is measurement vector given by

$$Z(k) = S(k + 1) - S(k) = J_I \cdot (\Delta r(k)), \quad (19)$$

and $H(k) \in \mathbb{R}^{m_s \times (m_s \times n_r)}$ is measurement matrix as

$$H(k) = \begin{bmatrix} \Delta r(k) & & & \\ & \ddots & & \\ & & \Delta r(k) & \\ & & & \Delta r(k) \end{bmatrix}_{m_s \times (m_s \times n_r)}. \quad (20)$$

In SVSF, (17) and (18) are denoted as state space equations of the robot vision system. The system estimation can be summarized as follows.

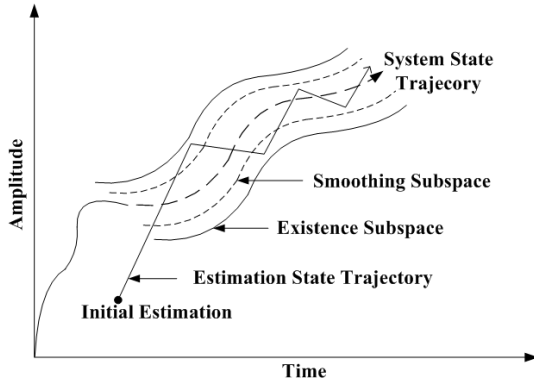


FIGURE 1. SVSF estimation concept.

First, the state estimation $\hat{X}(k | k - 1)$ and state error covariance $P(k | k - 1)$ of the system are calculated by

$$\hat{X}(k | k - 1) = \hat{X}(k), \quad (21)$$

$$P(k | k - 1) = P(k - 1) + Q(k - 1). \quad (22)$$

Second, by using the above state estimation $\hat{X}(k | k - 1)$ and the corresponding predictive measurement $\hat{Z}(k | k - 1)$, the measurement error $e_z(k | k - 1)$ can be calculated by

$$\hat{Z}(k | k - 1) = H(k)\hat{X}(k | k - 1), \quad (23)$$

$$e_z(k | k - 1) = Z(k) - \hat{Z}(k | k - 1). \quad (24)$$

Third, the gain $K(k)$ of SVSF which is a function of the prior measurement errors $e_z(k | k - 1)$ and posterior measurement errors $e_z(k - 1 | k - 1)$ can be obtained by

$$K(k) = H^+(k)\text{diag}[|e_z(k | k - 1)| + \gamma |e_z(k - 1 | k - 1)|] \circ \text{sat}(e_z(k | k - 1))\Psi \text{diag}(e_z(k | k - 1))^{-1}, \quad (25)$$

where $H^+(k)$ is the pseudo-inverse of the measurement matrix $H(k)$, γ is the convergence rate of SVSF, Ψ is a smooth boundary layer (SBL), the sign \circ represents the Schur product, and the symbolic function is defined as

$$\text{sat}(e_z(k | k - 1), \Psi_i) = \begin{cases} 1, & e_z(k | k - 1)/\Psi_i \geq 1 \\ e_z(k | k - 1)/\Psi_i, & 1 < e_z(k | k - 1)/\Psi_i < 1 \\ -1, & e_z(k | k - 1)/\Psi_i \leq -1. \end{cases} \quad (26)$$

The gain $K(k)$ is used to estimate the state $X(k | k)$ and update state error covariance matrix $\hat{P}(k)$ as

$$X(k | k) = X(k | k - 1) + K(k)e_z(k | k - 1), \quad (27)$$

$$P(k) = (I - K(k)H(k))P(k | k - 1)(I - K(k)H(k))^T + K(k)R(k - 1)K(k)^T, \quad (28)$$

where $I \in \mathbb{R}^{m_s n_r \times m_s n_r}$ is identify matrix.

Finally, the measurement estimation $\hat{Z}(k | k)$ and the measurement error $e_z(k | k)$ can be calculated by

$$\hat{Z}(k | k) = H(k)\hat{X}(k | k), \quad (29)$$

$$e_z(k | k) = Z(k) - \hat{Z}(k | k). \quad (30)$$

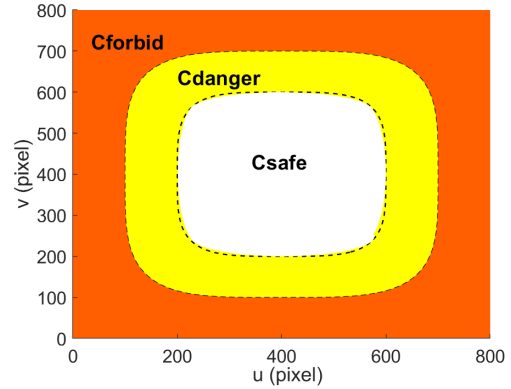


FIGURE 2. Hyperelliptic field constraints.

The estimation error is convergent, if

$$|e_z(k | k)| < |e_z(k - 1 | k - 1)|. \quad (31)$$

The proof is provided in detail in [41].

III. VISIBILITY CONSTRAINTS

It is difficult to obtain the control law of the robot visual servo when the target image features leave the camera FOV. To avoid this problem, a constraint function which is limited in the image plane is defined for each image feature.

In this article, a constraint function is introduced to limit the motion speed and the direction of image features. The image features in the safe area are not required to reaction. When the image features locate in the danger area, gentle measures reduce the image features' movement to the worse region. Enforcement measure is taken when it is necessary to drag image features out of forbidden areas. The constraint function reflects the relationship between the image feature coordinates and region boundary functions.

It is necessary to eliminate the absent features to maintain image features when they locate at the image edges in FOV. To maintain them, the image boundary area is defined in Fig.2. There are three FOV regions in this figure, i.e., the safe region C_{safe} shown as white, the danger region C_{danger} shown as yellow and the forbidden region C_{forbid} shown as orange. To make the boundary constraint smoother, consider the formula for an ellipse $\frac{x}{a}|^k + \frac{y}{b}|^k = 1$ (called a hyperellipse for $\kappa > 2$), which is similar to a rectangle with rounded corners, the image boundary area can be described by

$$S_{V_{safe}}(u_s, v_s) = \left| \frac{u_s}{\frac{W_{V_{safe}}}{2}(1 - m_V)} \right|^{\kappa_V} + \left| \frac{v_s}{\frac{H_{V_{safe}}}{2}(1 - m_V)} \right|^{\kappa_V} = 1, \quad (32)$$

$$S_{V_{danger}}(u_d, v_d) = \left| \frac{u_d}{\frac{W_{V_{danger}}}{2}(1 - m_V)} \right|^{\kappa_V} + \left| \frac{v_d}{\frac{H_{V_{danger}}}{2}(1 - m_V)} \right|^{\kappa_V} = 1, \quad (33)$$

where u_s and v_s are the pixel coordinates of the image feature $S_{V_{safe}}$ on the ellipse of safe boundary, u_d and v_d are the pixel coordinates of the image feature $S_{V_{danger}}$ on the ellipse of danger boundary, κ_V is the super-elliptic smoothing parameter to smooth the rounded corners of the constrained boundary, $H_{V_{safe}}$ and $W_{V_{safe}}$ are those of the ellipse of the safe boundary, $H_{V_{danger}}$ and $W_{V_{danger}}$ are the length and width of the ellipse of danger boundary, the width and height of the ellipse represent the plane limit of the image in pixels, m_V is the safety margin of visibility constraints to cope with possible errors and inaccuracies [42].

In this case, the value of adaptive gain F_i must be null at feature deactivation (Image feature S_i is in the safe region C_{safe}), and it increases as the constrained features vary from the safe region to the danger region. When the image feature moves to the forbidden region C_{forbid} , the value of adaptive gain $F_i = 1$. We address a continuous adaptive function F_i with the form as

$$F_i = \begin{cases} 0, & \text{if } S_i \in C_{safe} \\ \sqrt{\frac{f_{u_i}^2 + f_{v_i}^2}{2}}, & \text{if } S_i \in C_{danger} \\ 1, & \text{if } S_i \in C_{forbid}, \end{cases} \quad (34)$$

where $f_{u_i} \in [0, 1]$ and $f_{v_i} \in [0, 1]$ are weight factors, which can be denoted as

$$\begin{cases} f_{u_i} = 0.5 \times \left(1 - \tanh \left(\frac{1}{u_{d_i} - u_i} - \frac{1}{u_i - u_{s_i}} \right) \right) \\ \quad \times \left| \frac{u_{s_i} - u_i}{\min(|u_i - u_{\min}|, |u_i - u_{\max}|)} \right|, \\ f_{v_i} = 0.5 \times \left(1 - \tanh \left(\frac{1}{v_{d_i} - v_i} - \frac{1}{v_i - v_{v_i}} \right) \right) \\ \quad \times \left| \frac{v_{s_i} - v_i}{\min(|v_i - v_{\min}|, |v_i - v_{\max}|)} \right|, \end{cases} \quad (35)$$

where $u_i \in [u_{\min}, u_{\max}]$ and $v_i \in [v_{\min}, v_{\max}]$ are the pixel coordinates of the image feature S_i , u_{\min} , u_{\max} , v_{\min} and v_{\max} are the limits of image plane. The injection adaptive function F_i is represented in Fig.3.

Based on the velocity control law, FOV performance is maintained. Therefore, the velocity controller based on the FOV constraint can be rewritten as

$$\dot{i}(k) = -\lambda \cdot J_I^+(k) \cdot F_{uv}(k) \cdot e(k), \quad (36)$$

where $F_{uv}(k)$ is an imposed constraint function as

$$F_{uv}(k) = \begin{bmatrix} 1-\delta F_1(k) & & & & \\ & 1-\delta F_1(k) & & & \\ & & \ddots & & \\ & & & 1-\delta F_{m_s}(k) & \\ & & & & 1-\delta F_{m_s}(k) \end{bmatrix}_{2m_s \times 2m_s}, \quad (37)$$

where $\delta \in (0, 1)$ is a positive constant, which stands for the constraint degree.

To ensure the stability of the velocity controller based FOV constraints, some assumptions are taken into consideration.

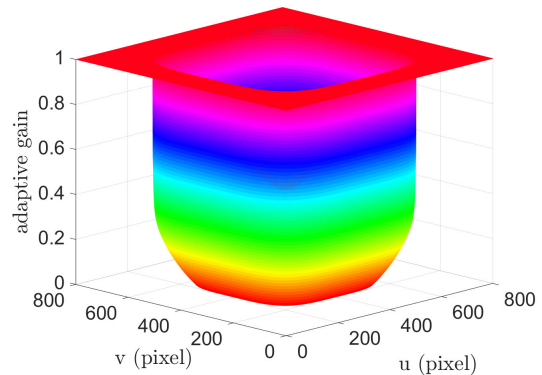


FIGURE 3. The value of adaptive gain.

Since image feature S is composed of four image points, $rank_{\max}(J_I J_I^+) = 6$, where $rank_{\max}$ denotes the maximum rank, and $J_I J_I^+$ has two null vectors that satisfy $\{J_I J_I^+ x = 0, x \in \mathbb{R}^8, x \neq 0\}$. Assuming that x does not fall in the null space of $J_I J_I^+$, we have $J_I J_I^+ > 0$ [1], [43]. We choose the Lyapunov function candidate as

$$L(k) = \frac{1}{2} \|e(k)\|^2. \quad (38)$$

The time derivative of the Lyapunov function is

$$\dot{L}(k) = (e(k))^T (\dot{e}(k)) = -\lambda (e(k))^T J_I(k) J_I^+(k) F_{uv}(k) e(k), \quad (39)$$

where $F_{uv}(k)$ is positive definite matrix, $J_I(k) J_I^+(k) > 0$ and $\lambda > 0$. Hence, we have $\dot{L}(k) < 0$, the control system is exponentially stable according to Lyapunov stability theorem.

IV. HYBRID ALGORITHM OF VISUAL SERVOING SYSTEM WITH FEATURE CONSTRAINTS

The IBVS by combing B-ELM with SVSF (B-ELM-SVSF) strategy with feature constraints is shown in Fig.4. In the presence of system noise and modeling uncertainties, the extraction of image features increases complexity and potential errors. B-ELM algorithm is adopted to estimate feature Jacobian matrix, but be vulnerable to noise. Therefore, the robustness and stability of SVSF is employed to further improve the estimation accuracy of Jacobian matrix. A visual constraint function is used in constructing the control law to effectively prevent feature points from being removed from FOV, which ensures the completion of the servo task. The algorithm is described as follows.

First, the region is judged according to the image feature information collected by the camera. Through the position information of the image feature, the proposed constraint function is introduced into the control law when the adaptive gain F_i is calculated.

Second, each element of the image features is taken as input, and the nonlinear off-line learning of B-ELM is carried out to obtain the approximation of each element of the feature Jacobian matrix.

Third, SVSF can estimate the system states online to obtain feature Jacobian matrix after calculating the output

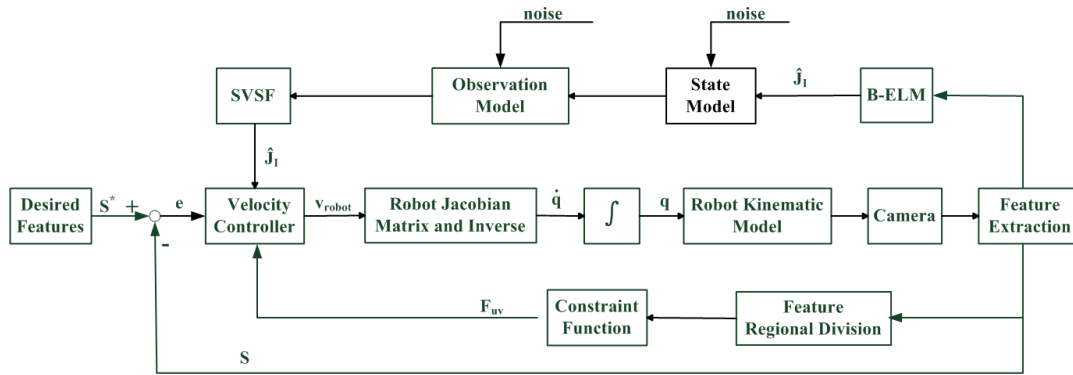


FIGURE 4. Algorithm structure diagram of B-ELM-SVSF with constraint function.

of the feature Jacobian matrix from B-ELM at the current moment, improve its vulnerability to external environments and uncertainties. The approximate Jacobian matrix based on re-estimation of SVSF is applied to the control law.

Finally, robot manipulator is driven from the initial position to the desired position by the modified velocity controller (36).

After each moving step, the new image features are extracted and the Jacobian matrix is re-estimated. It will drive the robot to move again until reaching the allowable error range of the desired image features.

In general, noise is assumed to be Gaussian white noise. However, in practice, due to noise interference, mechanical vibration, light intensity fluctuation, the state noise and measurement noise might be non-Gaussian or have some outliers in servo motion, thus it can be described by

$$v(k) = v_1(k) + v_2(k) \quad (40)$$

and

$$v(k) = v_1(k) + v_{\text{outlier}}(k), \quad (41)$$

where $v_1(k)$ is the Gaussian and white, $v_2(k)$ is also the Gaussian white noise with different statistical properties, and $v_{\text{outlier}}(k)$ is the outliers.

In the next session, we will discuss the robustness of the proposed method in dealing with Gaussian white noise and non-Gaussian noises such as (40) and (41) separately.

V. SIMULATION AND EXPERIMENTS

A. SIMULATION TESTS

In this section, the simulation is constructed with a 6-DOF robot where a camera is mounted on the end-effector and the static target consists of four circular feature points. The robotic manipulator conducted visual servo tasks in two cases, and the robustness and effectiveness of the proposed method is verified. In case 1, the robustness of the proposed B-ELM-SVSF-based IBVS method is evaluated in the presence of uncertainties and disturbances. Three different noises are introduced in the visual servo process respectively to make the robot move from the image feature captured

in the initial pose to the desired image feature. In case 2, the keeping ability of FOV is verified based on the proposed B-ELM-SVSF method as image features are chosen near FOV boundary.

In the simulation, the intrinsic parameters are set: the focal length of the camera is 8 mm and the image size is 800×800 . The feature points capture the center points of four circular disks. The proportional gain $\lambda = 0.5$, the sample interval $dt = 0.1$ s. 300 samples with different end-effector initial poses are used to train B-ELM to achieve sufficient approximation in the image plane. The number of hidden layer nodes is 82, and the mean square error (MSE) = 0.93, the running time is 0.953s.

1) SIMULATION CASE 1

We demonstrate the robustness of the proposed B-ELM-SVSF method based on estimation of Jacobian matrix, by comparing with traditional KF method (such as [44]). In the following subsections, three different cases, which contain different statistic characteristics of environmental noises, are assumed to make a better comparison. The initial joint angle of the robot is chosen as $(0, \pi/4, -\pi, 0, \pi/4, -\pi/4)^T$, the desired matrix of the image features $S^* = [400, 400, 200, 400, 200, 600, 400, 600]^T$. The initial and desired image features are shown by black circles and red circles, respectively. The servo motion stops when the error norm of image features is less than 0.5 pixel or the number of iterations reaches the maximum.

For the sub-case 1 in simulation case 1, Gaussian white noise is selected with its state noise covariance $Q = \text{diag}([0.1, \dots, 0.1]_{1 \times 48})$, and its measurement noise is $R = \text{diag}([0.1, \dots, 0.1]_{1 \times 8})$. The image feature trajectories of three comparison methods are shown in Figs.5(a) and 6(a). The feature trajectories of our proposed methods (B-ELM-SVSF) are nearly linear and smooth in Fig. 6(a). The feature trajectories of KF method are nonlinear due to the influence of noise as shown in Fig. 5(a). The image feature errors are convergent under the stop condition for all systems as shown in Figs. 5(b) and 6(b). The proposed method performs a faster convergence rate in Fig. 6(b), meanwhile, the feature errors

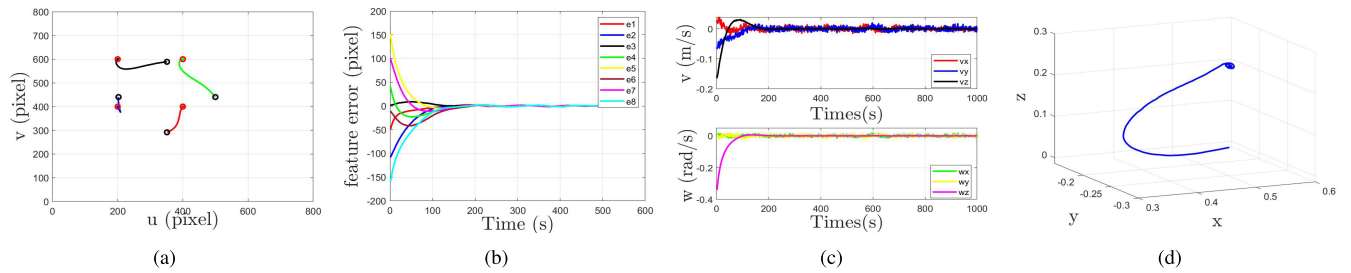


FIGURE 5. KF method in sub-case 1 in simulation case 1: (a) image feature trajectories (b) image feature errors (c) robot end-effector velocities (d) the trajectories of robot end-effector.

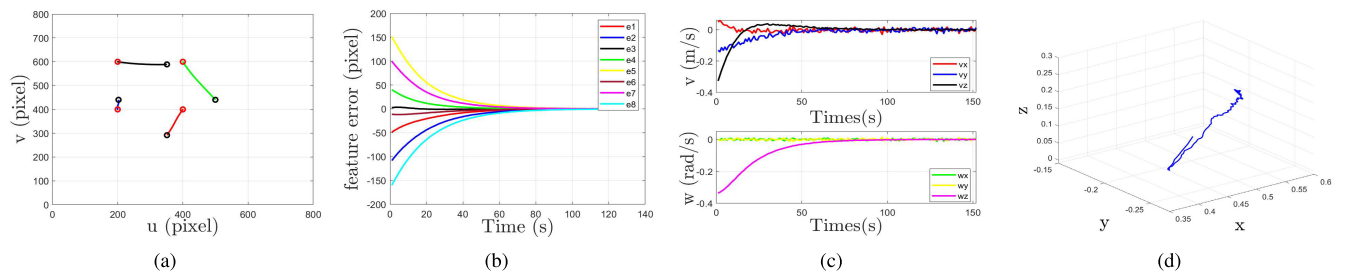


FIGURE 6. B-ELM-SVSF method in sub-case 1 in simulation case 1: (a) image feature trajectories (b) image feature errors (c) robot end-effector velocities (d) the trajectories of robot end-effector.

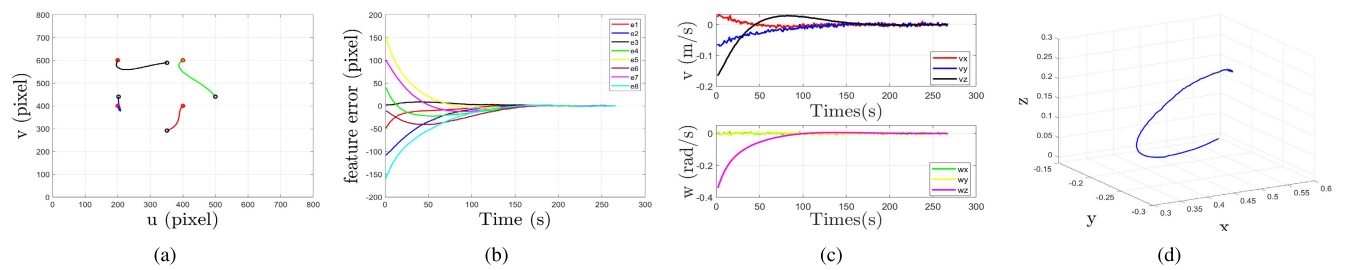


FIGURE 7. KF method in sub-case 2 in simulation case 1: (a) image feature trajectories (b) image feature errors (c) robot end-effector velocities (d) the trajectories of robot end-effector.

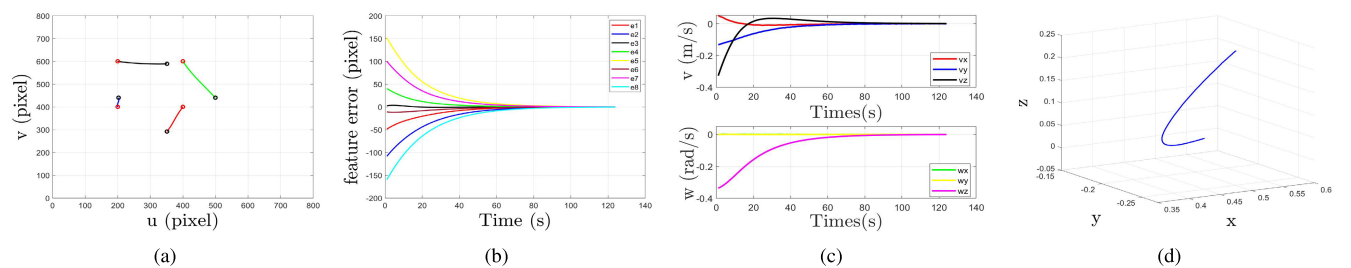


FIGURE 8. B-ELM-SVSF method in sub-case 2 in simulation case 1: (a) image feature trajectories (b) image feature errors (c) robot end-effector velocities (d) the trajectories of robot end-effector.

are decreased with exponentially. Some velocity components of the robot end-effector display slight vibration in both methods shown in Figs. 5(c) and 6(c). However, comparing with KF method in Fig. 6(d), the trajectory of the robot end-effector in Cartesian space performs less vibration and more preferred path by our method in Fig. 5(d).

For the sub-case 2 in simulation case 1, we introduce mix Gaussian noise in the measure process such as (40), in which $v_1(k) \in N(0, \delta_1)$, $v_2(k) \in N(0, \delta_2)$, $\delta_1^2 = \text{diag}([0.8, \dots, 0.8]_{1 \times 8})$, $\delta_2^2 = \text{diag}([0.3, \dots, 0.3]_{1 \times 8})$. As shown in Figs. 7 and 8, simulation results, which include the image features and their error curves, are basically similar

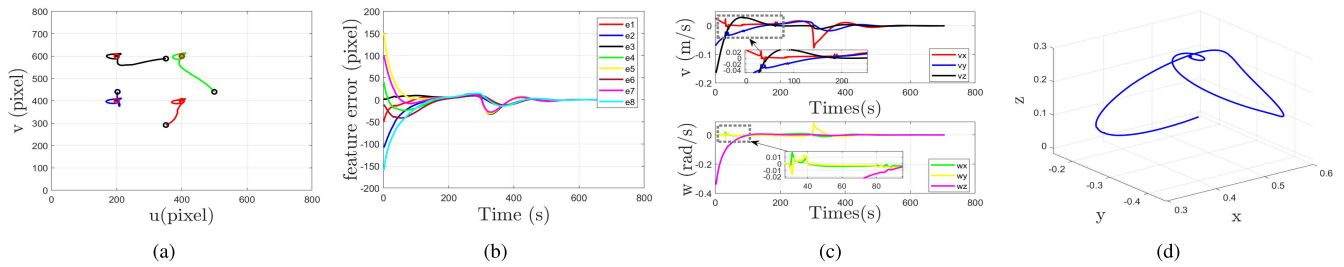


FIGURE 9. KF method in sub-case 3 in simulation case 1: (a) image feature trajectories (b) image feature errors (c) robot end-effector velocities (d) the trajectories of robot end-effector.

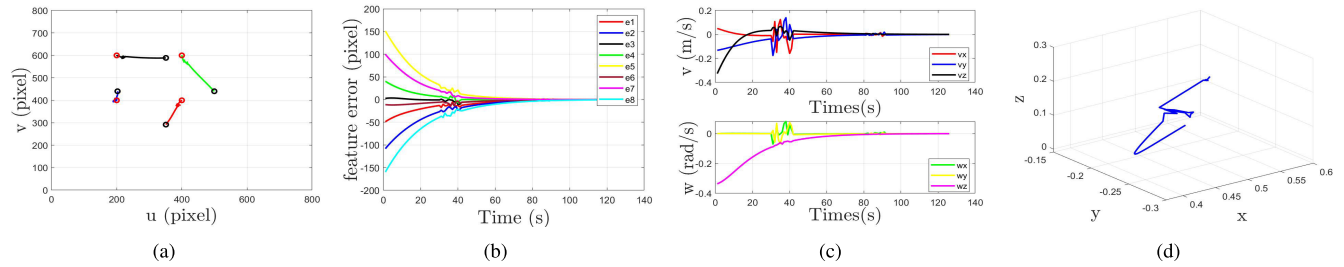


FIGURE 10. B-ELM-SVSF method in sub-case 2 in simulation case 1: (a) image feature trajectories (b) image feature errors (c) robot end-effector velocities (d) the trajectories of robot end-effector.

to those in sub-case 1. More specifically, line and angular velocities are continuous and smooth in the proposed method, but perform tiny fluctuation in KF method, which are shown in Figs. 7(c) and 8(c). In our method, trajectory of robot end-effector shows a less curvature in Cartesian space in Fig. 8(d).

For the sub-case 3 in simulation case 1, based on Gaussian white noise, 100 multiples of the noise are introduced as outliers into the simulation during 30-40s, 80-90s and 180-190s, respectively. We choose the state noise covariance is $Q = \text{diag}([0.00001, \dots, 0.00001]_{1 \times 48})$, and the measurement noise is $R = \text{diag}([0.00001, \dots, 0.00001]_{1 \times 8})$. In Figs. 9(a) and 9(b), it can be evidently observed that KF method distorts in both feature trajectories and feature errors. Besides, there are obvious abnormal fluctuations in the velocity curves except at the outliers in Fig. 9(c). KF method presents a worse path from the initial features to the desired features in the servo task as shown in Fig. 9(d). Figs. 10(a) and 10(b) illustrate the fluctuations feature trajectories and their errors when outliers occur. We observe that the velocity curves appear oscillation only during the time of outliers, as well as the trajectories of robot end-effector in Cartesian space.

Fortunately, the proposed method which relies on the B-ELM and SVSF methods has strong learning ability and robustness. It can be concluded that B-ELM-SVSF performs robustness of visual servoing task in the case of non-Gaussian noise.

2) SIMULATION CASE 2

We verify the performance of feature constraint between the proposed B-ELM-SVSF and traditional KF methods in two sub-cases. For sub-case 1 in simulation case 2, the state noise

covariance is $Q = \text{diag}([0.001, \dots, 0.001]_{1 \times 48})$, the measurement noise is $R = \text{diag}([0.001, \dots, 0.001]_{1 \times 8})$. We set the matrix of initial features S_{o1} and the matrix of desired features S_{o1}^* as

$$S_{o1} = \begin{bmatrix} 304.6 & 212.6 & 238.2 & 332.2 \\ 535.4 & 564.0 & 658.8 & 626.4 \end{bmatrix},$$

$$S_{o1}^* = \begin{bmatrix} 602.1 & 245.9 & 136.4 & 465.2 \\ 319.7 & 195.0 & 533.7 & 673.6 \end{bmatrix}.$$

The results without visibility constraint function are illustrated in Figs.11 and 12. The feature trajectories of KF method reach the desired pose, but beyond the FOV. In the actual operation, the servoing task fails directly due to the feature points leave the image plane. The B-ELM-SVSF method shows that the feature trajectories are tracked appropriately within FOV, and close to the edge of the image plane in Fig.12(a). Besides, Fig. 12(a) also verifies that the proposed method is able to constrained image feature to some extent. The feature errors are all convergent to 0.5 pixel in Figs. 11(b) and 12(b). Figs. 11(c) and 12(c) illustrate the continuous velocity of the robot. In Figs.11(d) and 12(d), the trajectory of robot end-effector in Cartesian space converges to the desired pose with smooth trajectories.

To show the performance of visibility constraint function, the matrix of initial features S_{o2} and the matrix of desired features S_{o2}^* are considered as sub-case 2 in simulation case 2.

$$S_{o2} = \begin{bmatrix} 304.6 & 212.6 & 238.2 & 332.2 \\ 535.4 & 564.0 & 658.8 & 626.4 \end{bmatrix},$$

$$S_{o2}^* = \begin{bmatrix} 602.1 & 245.9 & 136.4 & 465.2 \\ 319.7 & 195.0 & 533.7 & 673.6 \end{bmatrix}.$$

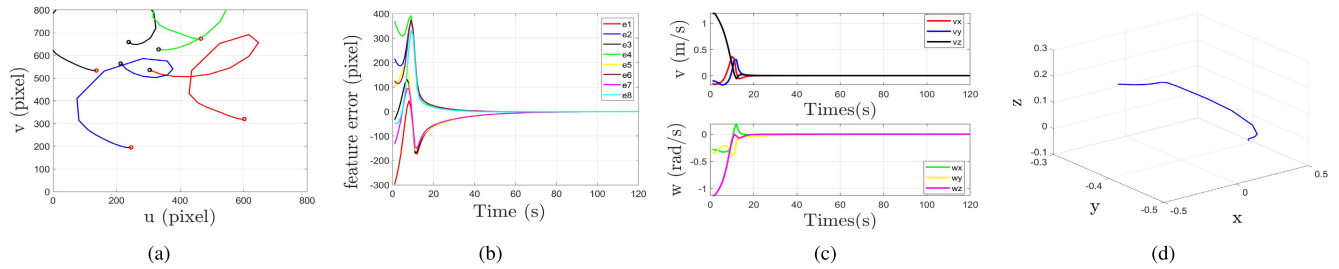


FIGURE 11. KF method in sub-case 1 in simulation case 2: (a) image feature trajectories (b) image feature errors (c) robot end-effector velocities (d) the trajectories of robot end-effector.

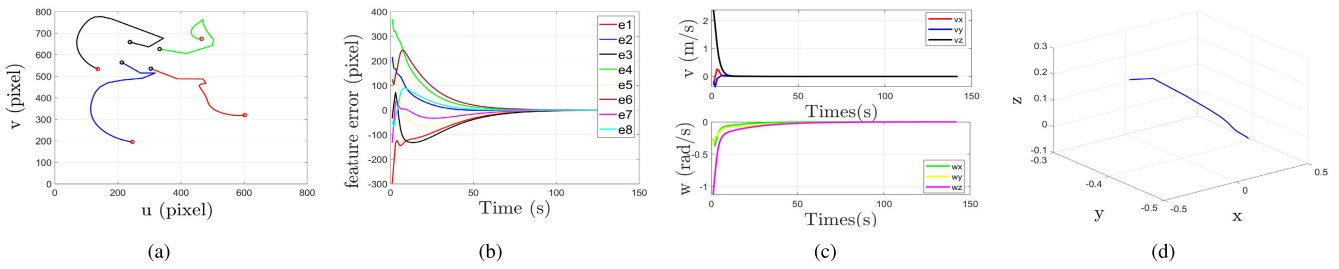


FIGURE 12. B-ELM-SVSF method in sub-case 1 in simulation case 2: (a) image feature trajectories (b) image feature errors (c) robot end-effector velocities (d) the trajectories of robot end-effector.

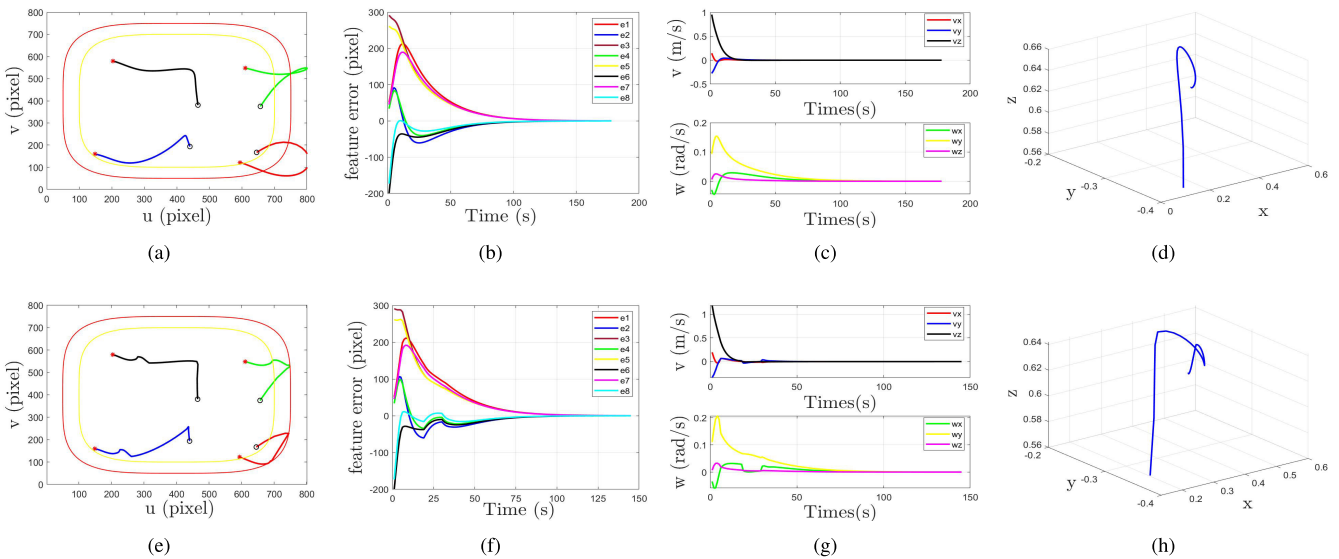


FIGURE 13. Results of sub-case 2 in simulation case 2 as 1st Row for B-ELM-SVSF without visibility constraint and 2nd Row for B-ELM-SVSF with visibility constraint. (a,e) feature trajectories, (b,f) the feature errors, (c,g) velocities of the end effector, (d,h) end effector trajectories.

Assume the height and the width be 700 pixels in the ellipse of forbid boundary, and 600 pixels in the ellipse of danger boundary. The hyperellipse smooth parameter $\kappa_V = 4$, safety margin $m_V = 0$. In this case, the state noise covariance is $Q = \text{diag}([0.004, \dots, 0.004]_{1 \times 48})$, the measurement noise is $R = \text{diag}([0.004, \dots, 0.004]_{1 \times 8})$.

In Fig. 13(a-h), the curves of the same servoing task both without and with FOV keeping are shown. The features move across C_{danger} and C_{forbid} beyond limitation of image plane

as shown in Fig. 13(a), which means that B-ELM-SVSF without constraint functions has risk to the failure of visual servoing. Besides, the proposed method provides FOV constraint to keep smooth transition between image regions shown in Fig.13(e). In Figs. 13(b) and (f), it is obvious that the errors of the image features entering the danger area C_{danger} and the forbid area C_{forbid} change in their profiles, while the features in the safe area are not affected basically. Furthermore, similar changes of velocities can be captured as

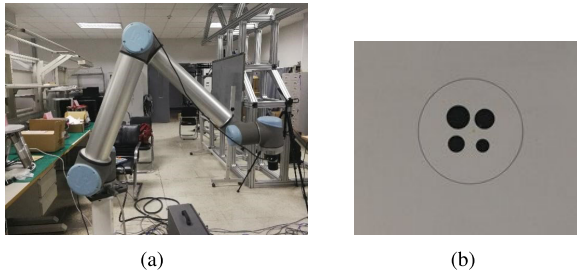


FIGURE 14. (a) Experiment environments with eye-in-hand configurations. (b) circular target.

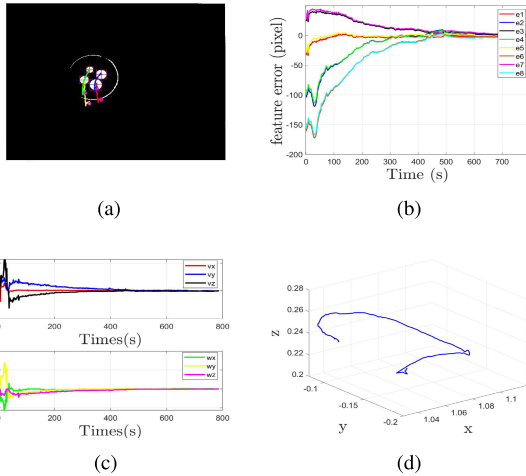


FIGURE 15. The proposed method in experiment case 1: (a) image feature trajectories (b) image feature errors (c) robot end-effector velocities (d) the trajectories of robot end-effector.

in Figs. 13(c) and (g). It is easy to ensure continuous velocity signals without any sudden changes. Therefore, implementing velocity constraint can move the features away from the target. With the proposed method, the trajectory of robot end-effector is continuous and reasonable in Fig. 13(h).

From the above simulation, it can be seen that B-ELM-SVSF method has a certain FOV constraint ability. However, feature points still escape from FOV in some cases. Therefore, we add the constraint function of image features to ensure that the servoing task can be completed for all cases.

B. EXPERIMENTAL TESTS

Our VS system consists of a UR10 robotic controller, a computer with Intel Core i5-65003, 20GHz CPU, 4GBs RAM for image processing, the computer communicates with controller by RS232C serial interface, and a UR10 6-DOF robotic manipulator with a Pixoel UI-1240LE-C-1 camera mounted at its end-effector is shown in Fig. 14(a). The object is a circular target with four small black-colored circular disks of different size on the table as shown in Fig. 14(b). The object images are captured by the camera at a rate of 25 Hz. The resolution is 1280 × 1024, and the center points of the small circular disks are used as feature points.

We consider translational and rotational movement of the camera in two cases to verify the effectiveness of our

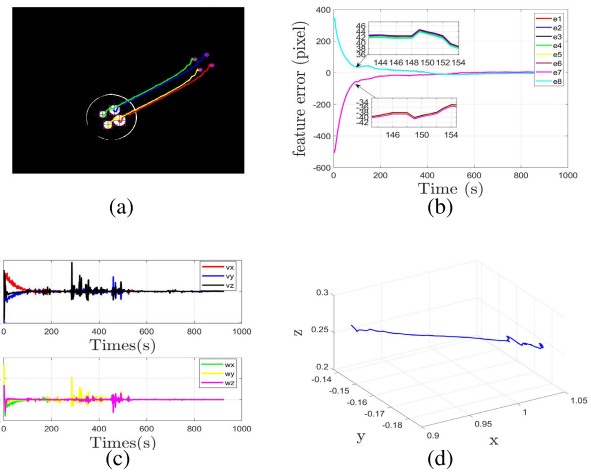


FIGURE 16. The proposed method in experiment case 2: (a) image feature trajectories (b) image feature errors (c) robot end-effector velocities (d) the trajectories of robot end-effector.

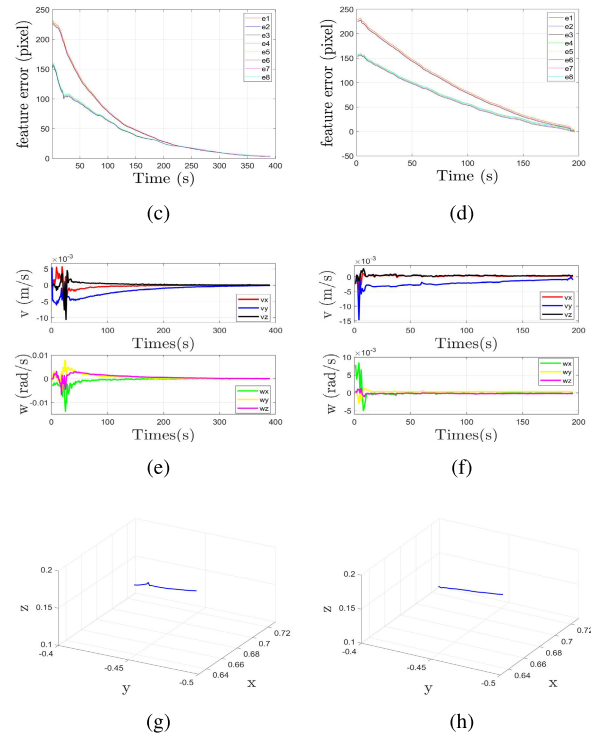
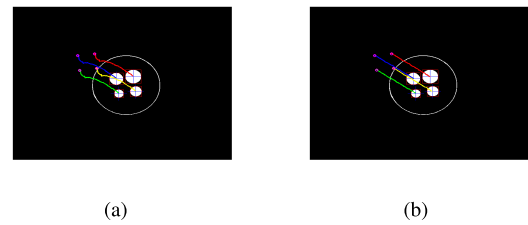


FIGURE 17. Results for experiment case 3 as 1st column for KF and 2nd column for B-ELM-SVSF. (a-b) feature trajectories, (c-d) the feature errors, (e-f) velocities of the end effector, (g-h) end effector trajectories.

uncalibrated-IBVS based on B-ELM-SVSF. For the first case of pure rotational movement, the initial and desired features

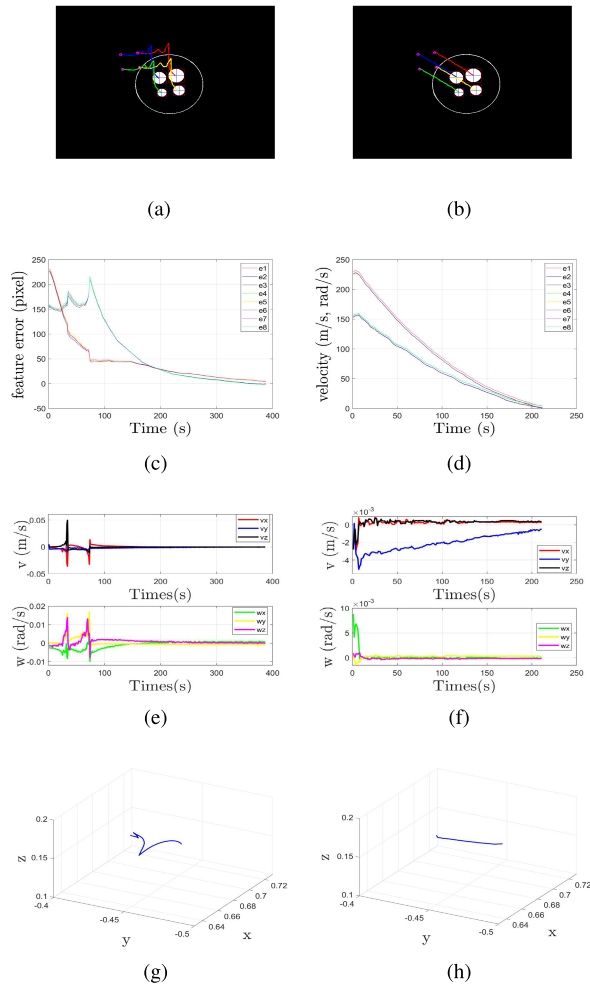


FIGURE 18. Results for experiment case 4 as 1st column for KF and 2nd column for B-ELM-SVSF. (a-b) feature trajectories, (c-d) the feature errors, (e-f) velocities of the end effector, (g-h) end effector trajectories.

are $S_{I_r} = (556.6, 630.0, 532.0, 560.2, 487.0, 655.0, 462.5, 585.3)^T$ and $S_{D_r} = (525.7, 530.1, 557.6, 463.3, 458.8, 498.5, 490.8, 431.9)^T$. In the experiment of case 2, the camera involves a low rotational angle and large translational movement. The initial and desired features are $S_{I_t} = (1102.0, 358.8, 1074.4, 293.8, 1037.3, 385.9, 1009.5, 320.9)^T$ and $S_{D_t} = (542.4, 739.1, 512.1, 676.8, 479.7, 768.4, 449.4, 706.2)^T$. The experimental results are shown in Figs. 15 and 16. In case 1, the feature trajectories are bent lines, and the image errors are gradually convergent to 8 pixels. The trajectory of robot end-effector is accomplished from the initial features to the desired features. For the case 2, the feature trajectories and robot trajectory in the Cartesian space are almost straight lines. The image errors converge from the initial features to the desired features. The velocities of robot end-effector decrease gradually in the servoing task. Although there are obvious vibrations under the influence of unknown factors during the process, the image trajectories are not affected.

In order to further test the robustness of our proposed method, we consider a simple servoing task to verify the

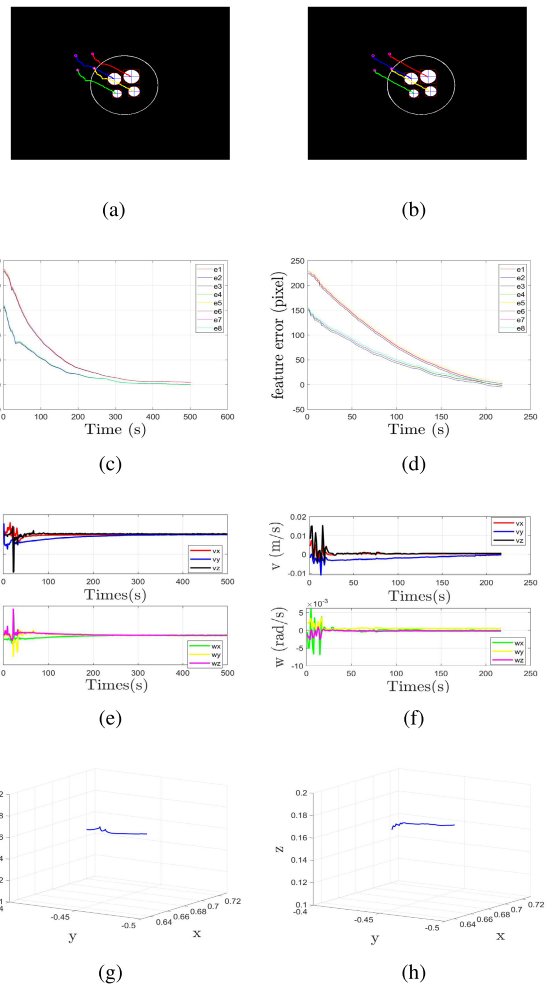


FIGURE 19. Results for experiment case 5 as 1st column for KF and 2nd column for B-ELM-SVSF. (a-b) feature trajectories, (c-d) the feature errors, (e-f) velocities of the end effector, (g-h) end effector trajectories.

robustness by introducing different statistical knowledge of environment noise comparing with KF method. The initial and desired matrix of the image features are given as $S_I = (447.8, 363.5, 351.7, 383.9, 467.3, 459.9, 370.6, 480.3)^T$ and $S_D = (685.1, 496.1, 588.0, 519.5, 708.9, 593.6, 611.6, 616.9)^T$. In the experiment of case 3, we choose Gaussian white noise with zero mean, the system noise variance is $Q = \text{diag}([0.0001, \dots, 0.0001]_{1 \times 48})$, and the observation noise variance $R = \text{diag}([0.001, \dots, 0.001]_{1 \times 8})$. In the experiment of case 4, the noise of image feature changes to the noise with zero mean and the covariance $R = \text{diag}([0.001, \dots, 0.001]_{1 \times 8})$. In the experiment of case 5, 10 multiples of noise is added at 30-40s on the basis of the experiment case 3.

The experiment results of case 3 are shown in Fig. 17. Image trajectories move to the allowable range of the desired features in the form of linear as same as the sub-case 1 in simulation case 1. The image errors gradually converge from the initial features to the desired features, the velocities of end-effector has obvious vibration at the beginning and then

decrease smoothly. The trajectory of end-effector is smooth in the Cartesian space, however, KF method performs a slight vibration. The experiment results of case 4 are shown in Fig. 18. It is noted that the image trajectories are not straight lines in KF method, the velocity curves appear twice abnormal fluctuations at 20-80s, the trajectory in Cartesian space is seriously affected by increasing noise. There are no discernible influence in the B-ELM-SVSF method. The image trajectories are still straight lines. Similarly, the robot trajectory is smooth under increasing. The experimental results of case 5 are shown in Fig. 19. The feature trajectories show almost straight lines in our method, while the trajectories of KF method is a bent line in Figs. 19(a) and (b). The image errors of two methods gradually decrease similar to Figs. 19(c) and (d). The velocities of end-effector perform distinct vibrations when outliers occur, and then gradually stable in Figs. 19(e) and (f). Figs. 19(g) and (h) show smoother curves of robot end-effector without outliers.

The experimental results show the robustness of the proposed method. From the comparative experiment of KF method, it shows that the method has a stronger robustness in the present of noise and disturbance.

VI. CONCLUSION

In this article, a novel IBVS system with hybrid control method has been proposed. The method approximates the feature Jacobian matrix through B-ELM and SVSF which is robust to camera calibration errors and feature noises. The B-ELM can quickly and effectively approximate the nonlinear relationship of the feature Jacobian matrix, while the SVSF plays a prominent role in overcoming disturbances such as environmental noise and mechanical errors. In order to avoid the task failures caused by image features beyond FOV, an effective constraint function was designed to adjust the motion speed according to the description of hyperelliptic boundary. Meanwhile, the trajectory of image features was effectively constrained to move within the boundary without abrupt change of speed. The simulations and experiments based on 6-DOF manipulator show that the proposed method is effective.

In this study, simulation results are presented to FOV constraint only, but we will focus on the application. Furthermore, the feature extraction in VS will be selected as diverse feature information in our future work.

REFERENCES

- [1] F. Chaumette and S. Hutchinson, "Visual servo control. I. Basic approaches," *IEEE Robot. Autom. Mag.*, vol. 13, no. 4, pp. 82–90, Dec. 2006.
- [2] F. Chaumette and S. Hutchinson, "Visual servo control. II. Advanced approaches [tutorial]," *IEEE Robot. Autom. Mag.*, vol. 14, no. 1, pp. 109–118, Mar. 2007.
- [3] S. Hutchinson, G. D. Hager, and P. I. Corke, "A tutorial on visual servo control," *IEEE Trans. Robot. Autom.*, vol. 12, no. 5, pp. 651–670, Oct. 1996.
- [4] D. I. Kosmopoulos, "Robust jacobian matrix estimation for image-based visual servoing," *Robot. Comput.-Integr. Manuf.*, vol. 27, no. 1, pp. 82–87, Feb. 2011.
- [5] B. Tao, Z. Gong, and H. Ding, "Survey on uncalibrated robot visual servoing control," *Chin. J. Theor. Appl. Mech.*, vol. 48, no. 4, pp. 767–783, 2016.
- [6] X. Zhang, Y. Fang, B. Li, and J. Wang, "Visual servoing of nonholonomic mobile robots with uncalibrated camera-to-robot parameters," *IEEE Trans. Ind. Electron.*, vol. 64, no. 1, pp. 390–400, Jan. 2017.
- [7] T. Li and H. Zhao, "Global finite-time adaptive control for uncalibrated robot manipulator based on visual servoing," *ISA Trans.*, vol. 68, pp. 402–411, May 2017.
- [8] M. Gridseth, O. Ramirez, C. P. Quintero, and M. Jagersand, "ViTa: Visual task specification interface for manipulation with uncalibrated visual servoing," in *Proc. IEEE Int. Conf. Robot. Autom. (ICRA)*, Stockholm, Sweden, May 2016, pp. 3434–3440.
- [9] J. Armstrong Piepmeier, G. V. McMurray, and H. Lipkin, "A dynamic Quasi-Newton method for uncalibrated visual servoing," in *Proc. IEEE Int. Conf. Robot. Autom.*, May 1999, pp. 1595–1600.
- [10] M. Josip, B. Mirjana, and C. Mojmil, "Comparison of uncalibrated model-free visual servoing methods for small-amplitude movements: A simulation study," *Int. J. Adv. Robotic Syst.*, vol. 11, no. 7, pp. 1–16, Jul. 2014.
- [11] M. Hao and Z. Sun, "A universal state-space approach to uncalibrated model-free visual servoing," *IEEE/ASME Trans. Mechatronics*, vol. 17, no. 5, pp. 833–846, Oct. 2012.
- [12] M. Bonkovic, A. Hace, and K. Jezernik, "Population-based uncalibrated visual servoing," *IEEE/ASME Trans. Mechatronics*, vol. 13, no. 3, pp. 393–397, Jun. 2008.
- [13] J. A. Piepmeier and H. Lipkin, "Uncalibrated eye-in-hand visual servoing," *Int. J. Robot. Res.*, vol. 22, no. 10–11, pp. 805–819, Oct. 2003.
- [14] J. A. Piepmeier, G. V. McMurray, and H. Lipkin, "Uncalibrated dynamic visual servoing," *IEEE Trans. Robot. Autom.*, vol. 20, no. 1, pp. 143–147, Feb. 2004.
- [15] Z. Gao and J. Su, "The estimation of image Jacobian matrix with time-delay compensation for uncalibrated visual servoing," *Control Theory Appl.*, vol. 26, no. 1, pp. 23–27, Jan. 2009.
- [16] J. M. Sebastián, L. Pari, L. Angel, and A. Traslosheros, "Uncalibrated visual servoing using the fundamental matrix," *Robot. Auto. Syst.*, vol. 57, no. 1, pp. 1–10, Jan. 2009.
- [17] L. Pari, J. M. Sebastian, A. Traslosheros, and L. Angel, "A comparative study between analytic and estimated image jacobian by using a stereoscopic system of cameras," in *Proc. IEEE/RSJ Int. Conf. Intell. Robots Syst.*, Taipei, Taiwan, Oct. 2010, pp. 6208–6215.
- [18] H. Li, Y. Shi, and G. Wang, "Vision-guided welding robot based on SVR-Jacobian estimator," *J. South China Univ. Technol. (Natural Sci. Ed.)*, vol. 41, no. 7, pp. 19–25, 2013.
- [19] J. Qian and J. Su, "Online estimation of image jacobian matrix by Kalman-Bucy filter for uncalibrated stereo vision feedback," in *Proc. IEEE Int. Conf. Robot. Autom.*, Washington, DC, USA, May 2002, pp. 562–567, doi: [10.1109/ROBOT.2002.1013418](https://doi.org/10.1109/ROBOT.2002.1013418).
- [20] J. Ma and Q. Zhao, "Robot visual servo with fuzzy particle filter," *J. Comput.*, vol. 7, no. 4, pp. 842–845, Apr. 2012.
- [21] A. Shademan, A.-M. Farahmand, and M. Jägersand, "Robust jacobian estimation for uncalibrated visual servoing," in *Proc. IEEE Int. Conf. Robot. Autom.*, Anchorage, AK, USA, May 2010, pp. 5564–5569.
- [22] J. Xin, L. Bai, and D. Liu, "Adaptive Kalman filter-based robot 6DOF uncalibrated vision positioning," *J. Syst. Simul.*, vol. 26, no. 3, pp. 586–591, 2014.
- [23] X. Zhong, X. Zhong, and X. Peng, "Robots visual servo control with features constraint employing Kalman-neural-network filtering scheme," *Neurocomputing*, vol. 151, pp. 268–277, Mar. 2015.
- [24] X. Zhong, X. Zhong, H. Hu, and X. Peng, "Adaptive neuro-filtering based visual servo control of a robotic manipulator," *IEEE Access*, vol. 7, pp. 76891–76901, 2019.
- [25] H.-B. Wang and M. Liu, "Design of robotic visual servo control based on neural network and genetic algorithm," *Int. J. Autom. Comput.*, vol. 9, no. 1, pp. 24–29, Feb. 2012.
- [26] X. Zhong, X. Zhong, and X. Peng, "Robust Kalman filtering cooperated elman neural network learning for Vision-Sensing-Based robotic manipulation with global stability," *Sensors*, vol. 13, no. 10, pp. 13464–13486, Oct. 2013.
- [27] T. Yüksel, "Intelligent visual servoing with extreme learning machine and fuzzy logic," *Expert Syst. Appl.*, vol. 72, pp. 344–356, Apr. 2017.
- [28] M. Kang, H. Chen, and J. Dong, "Adaptive visual servoing with an uncalibrated camera using extreme learning machine and Q-learning," *Neurocomputing*, vol. 402, pp. 384–394, Aug. 2020.
- [29] M. Ourak, B. Tamadazte, O. Lehmann, and N. Andreff, "Direct visual servoing using wavelet coefficients," *IEEE/ASME Trans. Mechatronics*, vol. 24, no. 3, pp. 1129–1140, Jun. 2019.

- [30] Y. Mezouar and F. Chaumette, "Path planning for robust image-based control," *IEEE Trans. Robot. Autom.*, vol. 18, no. 4, pp. 534–549, Aug. 2002.
- [31] L. Deng, F. Janabi-Sharifi, and W. J. Wilson, "Hybrid motion control and planning strategies for visual servoing," *IEEE Trans. Ind. Electron.*, vol. 52, no. 4, pp. 1024–1040, Aug. 2005.
- [32] X. Ding, Z. Du, Y. Lu, and S. Liu, "Visual trajectory planning for mobile robots based on hybrid artificial potential field," *J. Zhejiang Univ. (Eng. Sci.)*, vol. 50, no. 7, pp. 1298–1306, Jul. 2016.
- [33] G. Chesi, K. Hashimoto, D. Prattichizzo, and A. Vicino, "Keeping features in the field of view in eye-in-hand visual servoing: A switching approach," *IEEE Trans. Robot.*, vol. 20, no. 5, pp. 908–914, Oct. 2004.
- [34] A. Hajiloo, M. Keshmiri, W.-F. Xie, and T.-T. Wang, "Robust online model predictive control for a constrained image-based visual servoing," *IEEE Trans. Ind. Electron.*, vol. 63, no. 4, pp. 2242–2250, Apr. 2016.
- [35] M. Perez-Cisneros, G. Garcia-Gil, S. Vega-Maldonado, J. Arámburo-Lizárraga, E. Cuevas, and D. Zaldivar, "Applying BAT evolutionary optimization to image-based visual servoing," *Math. Problems Eng.*, vol. 2015, pp. 1–11, Jan. 2015, doi: 10.1155/2015/590138.
- [36] C. P. Bechlioulis, S. Heshmati-alamdari, G. C. Karras, and K. J. Kyriakopoulos, "Robust image-based visual servoing with prescribed performance under field of view constraints," *IEEE Trans. Robot.*, vol. 35, no. 4, pp. 1063–1070, Aug. 2019.
- [37] Y. Yang, Y. Wang, and X. Yuan, "Bidirectional extreme learning machine for regression problem and its learning effectiveness," *IEEE Trans. Neural Netw. Learn. Syst.*, vol. 23, no. 9, pp. 1498–1505, Sep. 2012.
- [38] A. Rajpal, A. Mishra, and R. Bala, "Fast digital watermarking of uncompressed colored images using bidirectional extreme learning machine," in *Proc. Int. Joint Conf. Neural Netw. (IJCNN)*, Anchorage, AK, USA, May 2017, pp. 1361–1366.
- [39] Y. Yang, X. Lin, Z. Miao, X. Yuan, and Y. Wang, "Predictive control strategy based on extreme learning machine for path-tracking of autonomous mobile robot," *Intell. Autom. Soft Comput.*, vol. 21, no. 1, pp. 1–19, Jan. 2015.
- [40] S. Habibi, "The smooth variable structure filter," *Proc. IEEE*, vol. 95, no. 5, pp. 1026–1059, May 2007.
- [41] S. A. Gadsden, S. Habibi, and T. Kirubarajan, "Kalman and smooth variable structure filters for robust estimation," *IEEE Trans. Aerosp. Electron. Syst.*, vol. 50, no. 2, pp. 1038–1050, Apr. 2014.
- [42] P. Muñoz-Benavent, L. Gracia, J. E. Solanes, A. Esparza, and J. Tornero, "Robust fulfillment of constraints in robot visual servoing," *Control Eng. Pract.*, vol. 71, pp. 79–95, Feb. 2018.
- [43] F. Chaumette, "Potential problems of stability and convergence in image-based and position-based visual servoing," in *The Confluence Vis. Control (Lecture Notes in Control and Information Sciences)*, vol. 237, D. Kriegman, G. Hager, and S. Morse, Eds. New York, NY, USA: Springer-Verlag, 1998, pp. 66–78.
- [44] G. R. Liu, Z. Huang, L. L. Han, and J. K. Bi, "Tracking of two dimensional based on Kalman filtering," *J. Zhengzhou Univ. (Eng. Sci.)*, vol. 34, no. 1, pp. 95–98, Jan. 2013.



XIAOLIN REN was born in Jilin, China, in 1985. She received the B.E. degree from the China University of Petroleum, China, in 2008, and the M.S. degree from the Jilin University of Technology, China, in 2012. She is currently pursuing the Ph.D. degree with the University of Chinese Academy of Sciences and the Changchun Institute of Optics, Fine Mechanics and Physics, Chinese Academy of Sciences, China. Since 2012, she has been a Laboratory Master in control science and engineering with the Changchun University of Technology, Changchun, China. Her research interests include robotics visual servoing control and intelligent control and high-precision machine control techniques.



HONGWEN LI was born in Sichuan, China, in 1970. He received the M.S. degree from the Jilin University of Technology, China, in 1996, and the Ph.D. degree from Jilin University, China, in 2007. From 1996 to 2002, he was an Associate Professor with the Jilin University of Technology. Since 2002, he has been with the Changchun Institute of Optics, Fine Mechanics and Physics, Chinese Academy of Sciences, China, where he is currently a Professor with the Department of Optical-Electronic Detection. His research interests include optical-electric sensor technologies, electric machines and drives, and high-precision machine control techniques.



YUANCHUN LI received the M.S. and Ph.D. degrees from the Harbin Institute of Technology, China, in 1987 and 1990, respectively. He is currently a Professor with the Changchun University of Technology, China. His research interests include complex system modeling, intelligent mechanical, and robot control.

• • •